PERGAMON

International Journal of Rock Mechanics and Mining Sciences 37 (2000) 143–160

International Journal of
Rock Mechanics
and Mining Sciences

www.elsevier.com/locate/ijrmms

Micromechanics of compressive failure and spatial evolution of anisotropic damage in Darley Dale sandstone

Xiang Yang Wu[b], P. Baud[a], Teng-fong Wong[a,*]

[a]*Department of Geosciences, State University of New York at Stony Brook, Stony Brook, NY 11794-2100, USA*
[b]*Institute of Geophysics, Chinese Academy of Sciences, Beijing, 100101, China*

Accepted 7 October 1999

Abstract

The micromechanics of compressive failure in Darley Dale sandstone (with initial porosity of 13%) was investigated by characterizing quantitatively the spatial evolution of anisotropic damage under the optical and scanning electron microscopes. Two series of triaxial compression experiments were conducted at the fixed pore pressure of 10 MPa and confining pressures of 20 and 210 MPa, respectively. For each series, three samples deformed to different stages were studied. Failure in the first series was by brittle faulting. In contrast, failure in the second series was ductile, involving shear-enhanced compaction and distributed cataclastic flow. In the ductile series, crack density and acoustic emission activity both increased with the development of strain hardening. The stress-induced cracking was relatively isotropic. In the brittle series, crack density increased with the progressive development of dilatancy, with spatial distributions indicative of clustering of damage at the peak stress and shear localization in the strain softening stage. Dilatancy was associated with significant anisotropy in stress-induced cracking, that was primarily due to intragranular and intergranular cracking with a preferred orientation parallel to the maximum principal stress. Compared with published data for Westerly granite and San Marcos gabbro (with porosities of the order of 1%) and for Berea sandstone (with porosity of 21%), there is an overall trend for the stress-induced anisotropy (in a sample deformed to near the peak stress) to decrease with increasing porosity. The sliding wing crack model was adopted to analyze the evolution of anisotropic damage, using a friction coefficient and fracture toughness inferred from stress states at the onset of dilatancy. Significant discrepancy exists between the model prediction and microstructural data on stress-induced anisotropy, which is possibly due to limitations intrinsic to the microscopy technique as well as the sliding wing crack model.

1. Introduction

Significant advances have been made in the fundamental understanding of the micromechanics of compressive failure in rock. It is now recognized that the macroscopic faulting process in a brittle rock actually involves a multiplicity of microcracks and its essential nature lies not only in the initiation and propagation of individual cracks but also in the interaction and coalescence of the crack population. In a seminal study, Hallbauer, Wagner and Cook [1] conducted optical microscope observations to elucidate the spatial evolution of cracking and development of shear localization in a compact quartzite. Subsequent studies using the scanning electron microscope (SEM) have provided additional details on the geometric attributes and anisotropy of stress-induced cracking [2,3] and the instability mechanisms associated with crack coalescence [4,5].

Earlier studies have focused on compact silicate rocks, such as Westerly granite and San Marcos gabbro. Dilatancy has been observed to arise from intragranular and intergranular cracking with a preferred orientation parallel to the maximum principal stress (σ_1). As stress is increased to near the peak, crack density as well as stress-induced anisotropy [6,7] increase significantly, with corresponding changes in elastic and

* Corresponding author. Tel.: +1-631-632-8212; fax: +1-516-632-8240.
E-mail address: tfwong@notes.cc.sunysb.edu (T. Wong).

1365-1609/00/$ - see front matter
PII: S1365-1609(99)00093-3

transport tensor properties [8,9]. In the strain softening stage, microcracking and acoustic emission activity begin to be localized along a macroscopic shear band [4,10,11]. A conceptual model widely used to analyze such micromechanical processes is the "sliding wing crack" [12–14]. The model considers the growth of "wing cracks" that initiate from tensile stress concentration at the tips of pre-existing cracks undergoing frictional slip. The fracture mechanics is such that increasing the stress causes the wing crack to propagate along a curved path and ultimately reach a stable orientation parallel to the direction of σ_1. With the accumulation of such anisotropic damage distributed throughout the rock, it will ultimately attain a critical state at which the multiplicity of cracks coalesce to develop a shear band.

Recently there has also been significant interest in the micromechanics of compressive failure in porous clastic rocks. In a recent study, Menéndez, Zhu and Wong [15] concluded that brittle faulting in the Berea sandstone (with an initial porosity of 21%) involves micromechanical processes quite different from those in a compact rock. Dilatancy and acoustic emission activity in the pre-failure stage seem to primarily involve intergranular cracking. Very little intragranular cracking was observed, except for isolated clusters of microcracks that radiated from grain contacts in a sample loaded to very near the peak stress. Stress-induced anisotropy was not appreciable in all pre-failure samples. It seems that compressive failure in such a cemented granular material hinges on the contact and fracture mechanics at impinging grains, that are not well captured in a wing crack model.

Siliciclastic rocks of a wide range of porosities are encountered in rock mechanics applications. Although previous studies have detailed the micromechanics of compressive failure in the compact and porous endmembers, there is a paucity of data on rocks of intermediate porosities. The objective of this study is to conduct such a microstructural study on the Darley Dale sandstone (with an initial porosity of 13%), the mechanical and transport properties of which have already been documented [16–18]. We adopted Menéndez, Zhu and Wong's [15] methodology to characterize quantitatively the overall damage and stress-induced anisotropy in samples that had been deformed at two different pressure conditions, corresponding to the two distinct failure modes of brittle faulting and cataclastic flow. In addition we used Hallbauer, Wagner and Cook's [1] approach to characterize the spatial distribution of damage and delineate the development of shear localization. Following Nemat-Nasser's [19] suggestion, we also derived analytic expressions to describe the evolution of anisotropic damage in the sliding wing crack model. To assess its applicability and limitation, the model's predictions are compared with microstructural data of Darley Dale sandstone as well as Westerly granite, San Marcos gabbro, and Berea sandstone.

2. Experimental procedure

2.1. Studied samples

The samples were cored from a block of Darley Dale sandstone, which is considered to be similar to the samples recently studied by Read et al. [16] and Wong et al. [17]. It has an average grain size (mean intercept length) of 0.22 mm, and model composition of: quartz 67%, feldspar 14%, mica 2%, and clay 6% [17]. The grains are sub-angular and poorly sorted, with size ranging from 0.08 mm to 0.8 mm [16]. The porosity varies somewhat from block to block. The seven samples in this study have initial porosities that range from 13.1 to 13.6%, with a mean of 13.4%.

2.2. Deformation experiments

Triaxial compression tests were performed on cylindrical samples (of diameter 18.4 mm and height 38.1 mm) saturated with distilled water. The samples were deformed at room temperature under "drained" conditions at a constant pore pressure of 10 MPa. Kerosene was used as confining pressure medium, and the nominal strain rate for all the triaxial experiments was 1.3×10^{-5} s^{-1}. Porosity change was determined from the pore volume change divided by the initial bulk volume of the sample, with an uncertainty of 0.1%. The axial strain was calculated using the axial displacement monitored by a transducer (DCDT), and the axial stress was calculated from the measurements of an external load cell adjusting for relative change of cross-sectional area of the sample. A piezoelectric transducer (PZT-7, 5 mm diameter, 1 MHz longitudinal frequency) was installed on the flat surface of a steel spacer attached to the jacketed sample to measure acoustic emission (AE) activity during the triaxial experiments. More details of the experimental procedure were presented by Wong et al. [17].

Samples at different stages of deformation were unloaded and retrieved from the pressure vessel for microscope observations and quantitative microstructural characterization. The deformation histories of the samples are summarized in Table 1. For reference, an unstressed sample (DD0) was also studied. The stress–strain curves of Darley Dale sandstone have good reproducibility, and the solid curves shown in Figs. 1, 2 and 3 are for the samples (WB3 and WD3) with the most deformation. For reference, the hydrostatic compaction data is also included as the dashed curve in Fig. 1.

Table 1
Stress history of the samples investigated in this study. Except for DD0, all samples were deformed in conventional triaxial compression tests at a fixed pore pressure of $P_p = 10$ MPa under drained conditions. The stress, strain and porosity change are maximum values attained before the sample was unloaded and retrieved from the pressure vessel

Sample	Differential stress (MPa) $\sigma_1-\sigma_3$	Effective mean stress (MPa) $(\sigma_1+2\sigma_3/3-p_P$	Effective pressure (MPa) σ_3-P_p	Axial strain (%)	Porosity reduction (%)	Comments
DD0	0	0	0	0	0	Unstressed
WD1	262	287	200	1.65	2.75	Just beyond C^*
WD2	382	327	200	3.96	3.75	Distributed cataclastic flow
WD3	457	352	200	9.49	4.98	Distributed cataclastic flow
WB1	118	49	10	1.24	0.31	Between C' and peak stress
WB2	124	51	10	1.37	0.16	Close to the peak stress
WB3	99	43	10	1.87	−0.57	Post-peak, with a shear band

Two suites of triaxially compressed samples were deformed at constant confining pressures ($\sigma_2 = \sigma_3 = P_c$) of 20 and 210 MPa, respectively. Since the pore pressure P_p was fixed at 10 MPa, the corresponding effective pressures (P_c-P_p) were 10 and 200 MPa, respectively. If the overall compaction was solely controlled by the hydrostatic stresses, then porosity changes in triaxial compression tests should coincide with the hydrostat in Fig. 1. Deviations from the hydrostat would imply that the porosity change is dependent on both the hydrostatic and deviatoric stresses. At an effective pressure of 200 MPa, the porosity reduction curve coincided with the hydrostat up to a differential stress of about 260 MPa. When the differential stress was increased beyond this point (marked by C^* in Fig. 1), there was an *accelerated* decrease in porosity in comparison to the hydrostat. This phenomenon is referred to as "*shear-enhanced compaction*" [17,20].

The sample WD1 was retrieved soon after it had been loaded to beyond C^*. This development of shear-enhanced compaction is accompanied by strain hardening, evident in the stress–strain curve (Fig. 2). Previous microstructural studies have shown that shear-enhanced compaction in a porous sandstone arises from grain crushing and pore collapse, manifested by

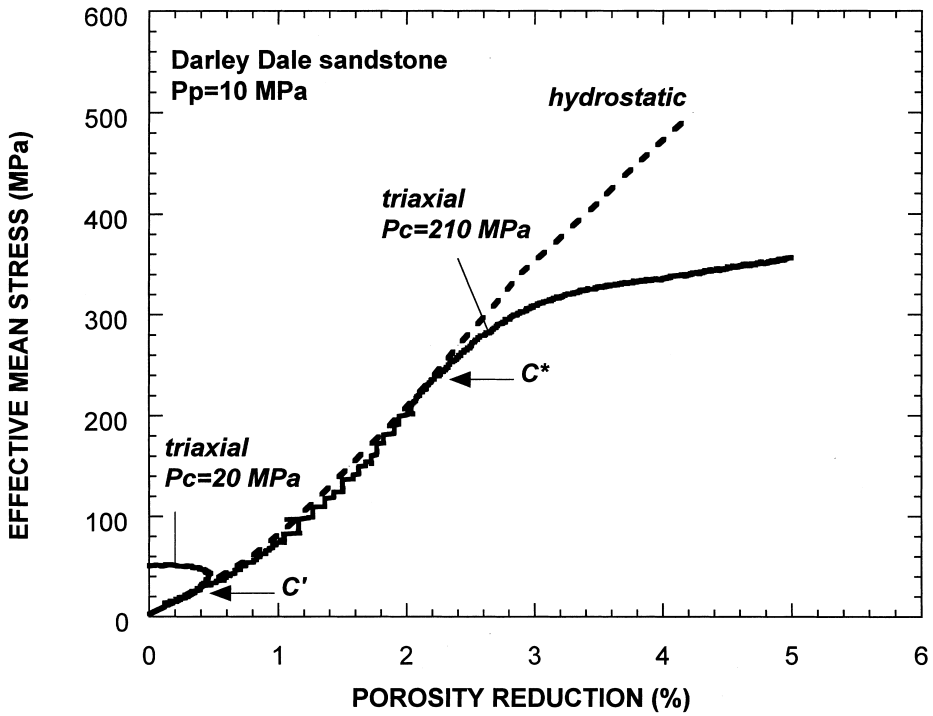

Fig. 1. Effective mean stress $(\sigma_1+2\sigma_3)/3-P_p$ vs porosity reduction for the two suites of samples showing the peak stresses attained by the samples before they were unloaded. For reference the hydrostat is also shown. The critical effective mean stresses for the onset of shear-enhanced compaction (C^*) and for the onset of dilatancy (C') are indicated.

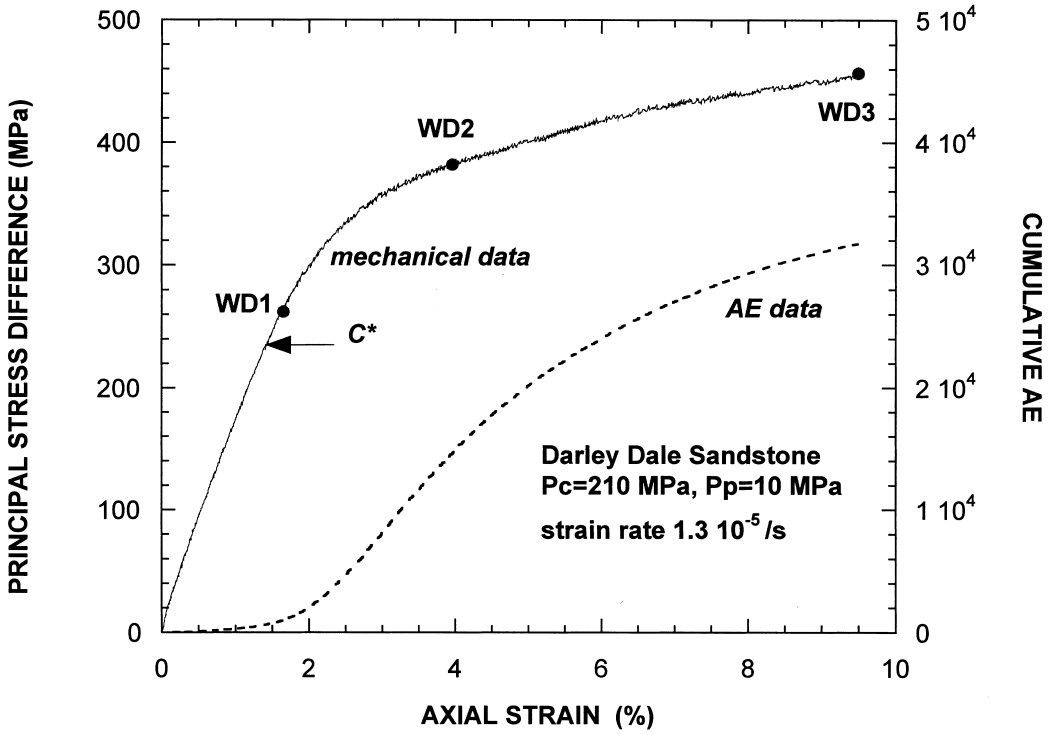

Fig. 2. Principal stress difference σ_1–σ_3 vs axial strain for the triaxially compressed samples of the WD-series with indication of the peak stresses attained by the samples. Acoustic emission activity is indicated by the dashed curve.

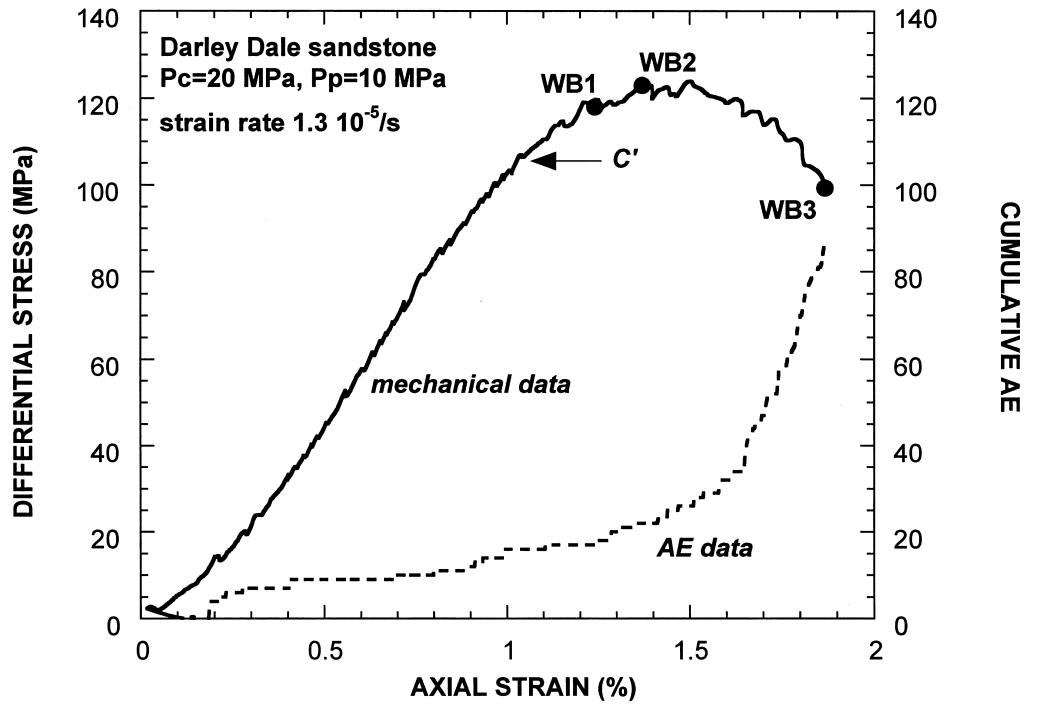

Fig. 3. Principal stress difference σ_1–σ_3 vs axial strain for the triaxially compressed samples of the WB-series with indication of the peak stresses attained by the samples. Acoustic emission activity is indicated by the dashed curve.

intensive AE activity (dashed curve in Fig. 2). Even though the last sample WD3 of this suite had an axial strain of close to 10%, no shear localization is evident and therefore the deformation was accommodated by distributed cataclastic flow.

In contrast, the porosity change behavior at an effective pressure of 10 MPa was such that at a differential stress of about 30 MPa, we began to observe the compaction to *decelerate* in comparison to the hydrostat. This stress state (marked by the point C' in Fig. 1) corresponds to the onset of dilatancy. Beyond C', the differential stress reached a peak value of 125 MPa, after which there was a gradual stress drop and strain softening (Fig. 3), and the sample ultimately failed by shear localization. The pre-failure sample WB1 was loaded to about half way between C' and the peak stress. The sample WB2 was unloaded as soon as the peak stress was attained, before the onset of shear localization. The sample WB3 was deformed well into the post-peak stage with a fully developed shear band. Our loading system is sufficiently stiff that the post-peak deformations were stable.

2.3. Optical and scanning electron microscopy

The deformed samples were first impregnated with epoxy and then sawed along a plane parallel to the axial direction into two halves. In sample WB3, care was taken to saw along a plane normal to the plane of localization. For each deformed sample, a crack section (25.4 mm in diameter and about 100 μm thick) was then prepared following the procedure outlined by Richter and Simmons [21]. The sections were then ion-milled [22] and sputter-coated with 0.02 μm of gold-palladium. Detailed observations of the damage were performed with a JEOL 5300 scanning electron microscope (SEM) with a voltage of 30 KV. All micrographs shown here are backscattered electron images.

Since an important objective was to characterize the spatial evolution of anisotropic damage, it was desirable to perform quantitative microstructural analysis over a relatively large portion of the crack section. For each sample, the spatial distribution of crack density over a total area of 11×11 mm^2 was characterized. The square area centrally located in a crack section is further divided into 11×11 subregions, each of which has an area of 1×1 mm^2. Using stereological techniques [23,24], we counted the number of crack intersections with a test array of 10 parallel lines spaced at 0.1 mm (about 1/3 of the average grain size) apart (Fig. 4). Measurements were made in two orthogonal directions parallel and perpendicular to σ_1, respectively. We denote the linear intercept density (number of crack intersections per unit length) for the array oriented parallel to σ_1 by $P_L^{\parallel}$, and that for the perpendicular array by $P_L^{\perp}$.

The stereological measurements were performed under an optical microscope interfaced with an automated image analysis system. The reflected images were all acquired at a magnification of 100×. For each sample, 121 pairs of stereological parameters ($P_L^{\parallel}$ and $P_L^{\perp}$) were measured to map out the spatial evolution of damage and stress-induced anisotropy. Previous studies [4,5,7] have demonstrated that since the spatial distribution of damage is approximately axisymmetric in a triaxially compressed sample, the crack surface area per unit volume (S_V) can be inferred from linear intercept measurements along two orthogonal direction

$$S_V = \frac{\pi}{2} P_L^{\perp} + \left(2 - \frac{\pi}{2}\right) P_L^{\parallel} \tag{1}$$

and the anisotropy of crack distribution can be characterized by the parameter

$$\Omega_{23} = \frac{P_L^{\perp} - P_L^{\parallel}}{P_L^{\perp} + (4/\pi - 1) P_L^{\parallel}} \tag{2}$$

that represents the ratio between the surface area of cracks parallel to σ_1 and the total crack surface area.

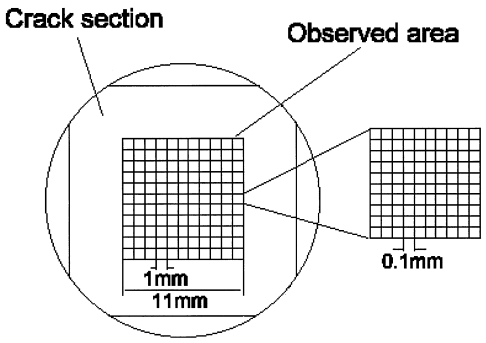

Fig. 4. Schematic diagram of a crack section showing the 121 subregions in which stereological measurements of crack density were conducted using orthogonal arrays of linear intercepts.

3. Microscopic observation of damage evolution

3.1. The WD-series: shear-enhanced compaction and cataclastic flow

For reference, we show in Fig. 5(a) a micrograph of the undeformed sample DD0. A number of grain boundaries were observed to be partially cracked. In addition, relatively short intragranular cracks were also observed along cleavages of the feldspar grains. Clay and cement are distributed heterogeneously in the pore space.

In the sample WD1 that was deformed to just

beyond the onset of shear-enhanced compaction, some intergranular cracks were observed. Many intragranular cracks were also observed in feldspar grains, often as parallel arrays along cleavages. The onset of grain crushing is indicated by isolated clusters of intragranular cracks radiating from grain contacts (Fig. 5(b)). Such "Hertzian fractures" have previously been observed during grain crushing and cataclastic flow in several other types of sandstone [15,25]

In the sample WD2, the development of shear-enhanced compaction is manifested by a larger number of crushed grains. The intense cracking mostly initiated as Hertzian fractures at grain contacts or as cleavage crack arrays in feldspar grains. In the sample WD3 that was deformed to about 9.5% of axial strain, intensive grain crushing was distributed throughout the sample (Fig. 5(c)). Many of the pores collapsed and the pore space was filled with comminuted particles (Fig. 5(d)).

3.2. The WB-series: dilatancy and shear localization

The pre-failure sample WB1 was deformed to half way between the onset of dilatancy and peak stress. The few intergranular cracks observed in this sample are somewhat longer and tend to be preferentially aligned sub-parallel to σ_1. Cleavage cracks in feldspar grains also appear to be longer and with somewhat wider apertures. In the sample WB2 deformed to close to the peak stress, an appreciable increase in the numbers of intergranular and intragranular cracks were observed sub-parallel to σ_1 (Fig. 6(a)). Many of these cracks developed along grain boundaries between quartz grains and along cleavages in feldspar grains. A few transgranular cracks extending over two to three grains were also observed.

In the post-peak sample WB3, shear localization developed along a curved band with angles ranging from 25° to 38° to σ_1. While damage in areas outside the shear band is qualitatively similar to that observed

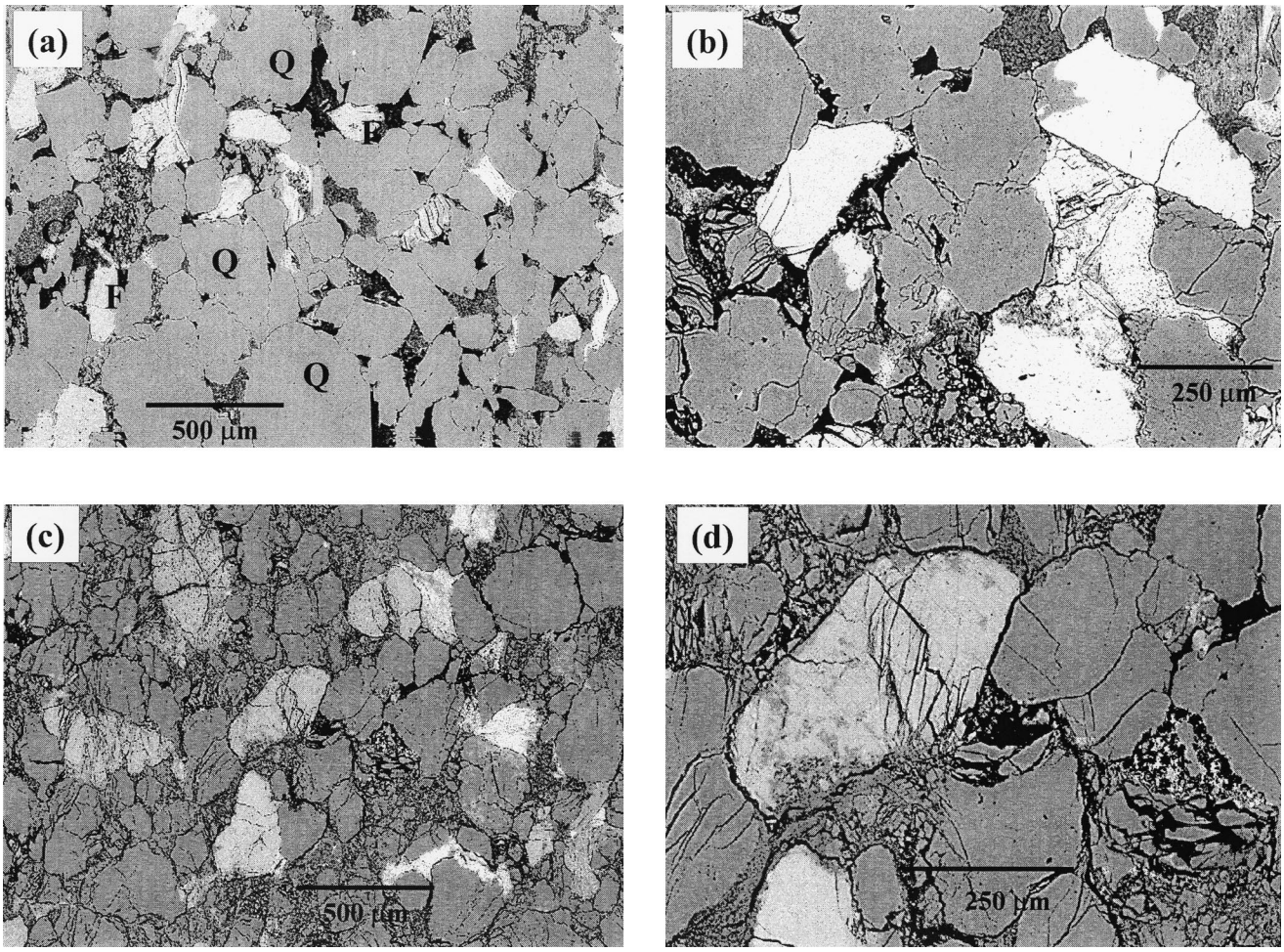

Fig. 5. (a) SEM micrograph of the unstressed sample DD0. The main mineralogical components are indicated: quartz (Q), clay (C) and feldspar (F). (b) Onset of grain crushing observed in sample WD1 that was triaxially compacted to just beyond the critical stress level C^*. (c) Extensive development of grain crushing and pore collapse as observed in the sample WD3 under relatively low magnification. (d) Details of (c) revealed at a higher magnification. The σ_1 direction is vertical in these SEM micrographs.

in WB2, the shear band itself was subjected to significantly more intense cracking. Along the shear band, over 70% of the discontinuity ran along grain boundaries (Fig. 6(b)) and the rest were formed either by coalescence of intragranular crack arrays in quartz and cleavage crack arrays in feldspar, or by grain crushing (mostly in the upper and lower ends of the shear band) (Fig. 6(c)). The shear band extended to a maximum width of two to three grains, although there are relatively narrow portions of it that cut through intergranular cracks.

3.3. Crack density, AE activity, and stress-induced anisotropy

The mean and standard deviation values of the stereological parameters (for the total observation area of 11×11 mm^2) are compiled in Table 2. The data illustrate how the overall damage evolved with deformation. They also provide first-order information on anisotropy and spatial heterogeneity of the damage. Two features of the WB-series should be noted (Fig. 7(a)). First, $P_L^{\perp}$ is significantly greater than $P_L^{\parallel}$ in WB2 and WB3 (both inside and outside the shear band), indicating that after the onset of dilatancy stress-induced cracking evolved in an anisotropic pattern, with a preferred orientation parallel to σ_1. Second, the density of microcracking progressively increased with deformation. The crack density $P_L^{\perp}$ increased by a factor of $\sim$5 at the peak stress. In the post-peak sample, pronounced enhancement of cracking was observed in the shear band, with a value of $P_L^{\perp}$ greater than that in the unstressed sample by an order of magnitude.

For the WD-series, the crack density also increased progressively with the development of shear-enhanced compaction and strain hardening. The linear crack intercept densities as functions of the axial strain follow approximately linear trends (Fig. 7(b)). The stereological measurements in two orthogonal directions show that the differences between $P_L^{\perp}$ and $P_L^{\parallel}$ in the three WD samples are comparable to that in the

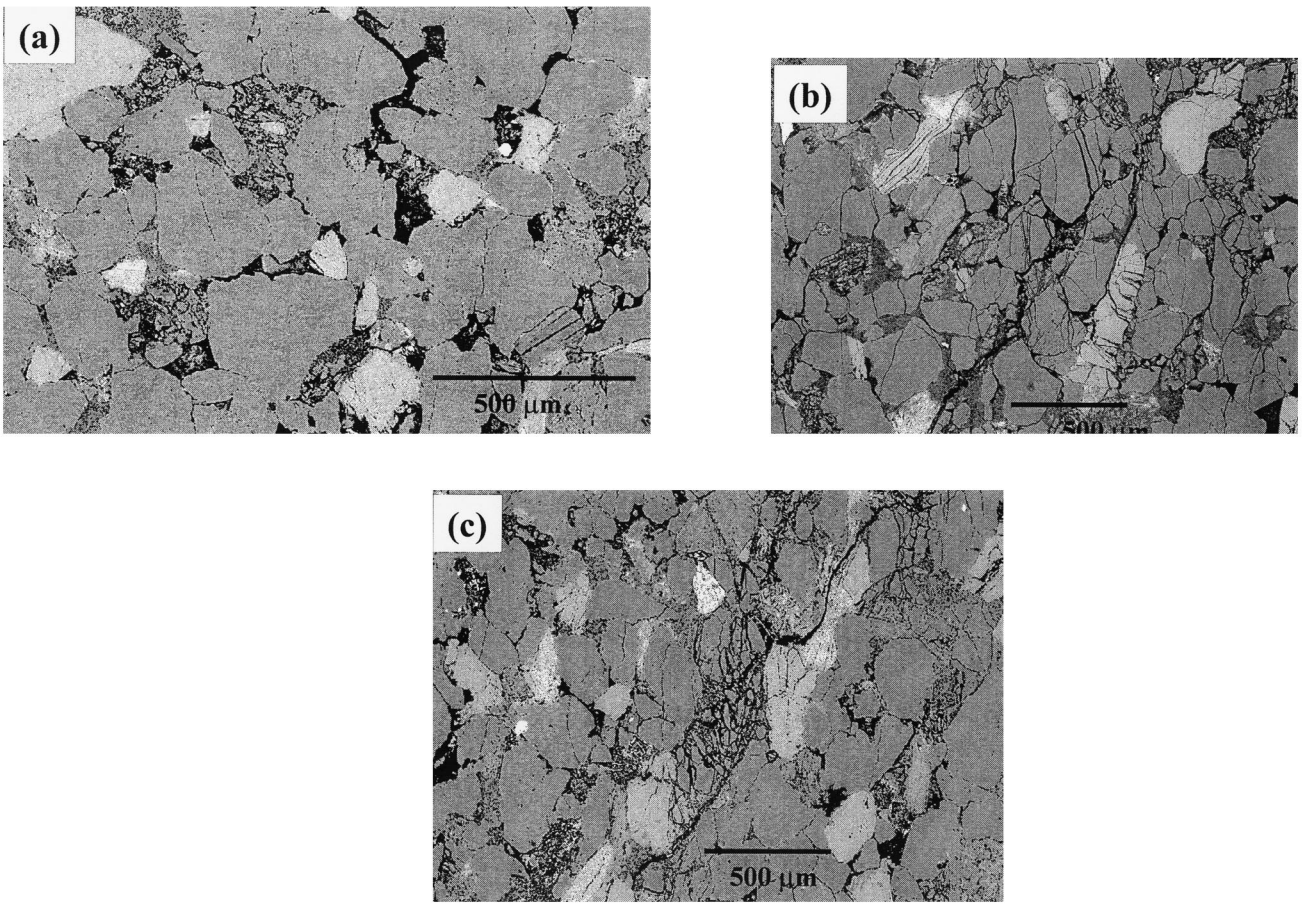

Fig. 6. (a) Stress-induced cracking in sample WB2 loaded to near the peak stress. (b) Part of the shear band that developed in the post-peak sample WB3. In this region, shear localization primarily occurred along grain boundary cracks. (c) Development of a shear band in the post-failure sample WB3, in a region that involved grain crushing. The σ_1 direction is vertical in these SEM micrographs.

unstressed sample (Table 2). This implies that stress-induced cracking was relatively isotropic during cataclastic flow.

Although the crack densities in the WB- and WD-series (as indicated by stereological measurements) are comparable in magnitude, deformation in the WB-series (Fig. 2) is associated with AE activity that is lower than that in the WD-series (Fig. 3) by as much as two orders of magnitude. This is possibility due to a significantly higher efficiency in the generation of AE events by Hertzian fracture and grain crushing during shear-enhanced compaction in the WD-series. The stereological and AE data show that there is a strong correlation between crack density and AE activity in the WD-series (Fig. 8).

3.4. Spatial evolution of anisotropic damage

While the standard deviation values of $P_L^{\perp}$ and $P_L^{\parallel}$ represent scalar measures of the spatial heterogeneity of damage in the stressed samples, they do not provide detailed information on the spatial evolution of damage. To visualize the spatial distribution of crack density in each sample, contour plots of the stereological measurements of the 121 sub-regions are presented in Figs. 9 and 10. The stereological data can also be analyzed in terms of specific surface area, which is directly proportional to the energy dissipated by the microcracking processes. Eq. (2) was used to evaluate the values of S_V, and the spatial distribution is visualized by contour plots (Fig. 11).

Two features of the spatial evolution of damage in the WB-series are worth noting. First, spatial heterogeneity increased with deformation. The sample WB-2 deformed to near the peak stress show clusters of enhanced cracking, and pronounced enhancement of damage was localized in the shear band of the post-peak sample WB-3. Second, in each sample the spatial distributions of crack densities in two orthogonal directions are correlated in the sense that sub-regions with high values of $P_L^{\perp}$ are usually associated with high values of $P_L^{\parallel}$ (Fig. 9).

In the WD-series, the stressed samples show similar spatial correlation between $P_L^{\perp}$ and $P_L^{\parallel}$ values. While the damage seems to become more clustered in the highly deformed samples, shear localization is absent even in WD3 that has accumulated an axial strain of 9.5% (Fig. 10) and crack density about twice of WB3 that failed by shear localization (Fig. 11).

4. Discussion

4.1. Micromechanics of compressive failure: comparison of Darley Dale and Berea sandstone

A sandstone for which the micromechanics of compressive failure has been investigated in detail is the Berea sandstone [10,15], which has an initial porosity significantly higher than the Darley Dale. Notwithstanding the differences in porosity, the ductile failure behavior is similar in that the development of shear-enhanced compaction in both sandstones arises from comminution and pore collapse. However, there is also a difference that is possibly related to modal composition. Since the Darley Dale sandstone has a higher percentage of feldspar grains, cleavage cracking within feldspar played an important role in the initiation of grain crushing (Fig. 5(c) and (d)). In contrast, Hertzian fracture seems to be the primary mechanism for the initiation of grain crushing in Berea sandstone. Since the development of Hertzian fracture is sensitive to the remotely applied stress field [26], there is a strong tendency for the stress-induced cracks to align with σ_1, which may explain why ductile deformation in Berea sandstone resulted in a more pronounced stress-induced anisotropy [10].

As for the development of brittle faulting, this study reveals key similarities and differences in the micromechanical processes operative in the two sandstones. In

Table 2
Quantitative microstructural data of unstressed and deformed samples. Crack densities were measured along linear intercepts perpendicular and parallel to the direction of σ_1, corresponding to the radial and axial directions, respectively. For each sample, linear intercept densities for 11 × 11 sub-regions of 1 mm^2 area were measured, and the mean and standard deviation of the 121 measurements are tabulated below. For the post-peak sample WB3 which failed by shear localization, the bracketed values are data measured inside the shear band

Darley Dale sandstone sample	Crack density for linear intercepts perpendicular to σ_1 $P_L^{\perp}$ (mm^{-1})	Crack density for linear intercepts parallel to σ_1 $P_L^{\parallel}$ (mm^{-1})	Crack area per unit volume S_v (mm^2/mm^3)	Anisotropy factor Ω_{23}
DD0	0.54 ± 0.30	0.45 ± 0.26	1.04	0.14
WD1	1.97 ± 0.51	1.27 ± 0.30	3.64	0.30
WD2	5.25 ± 1.62	4.65 ± 1.59	10.24	0.09
WD3	11.39 ± 1.97	10.67 ± 2.87	22.47	0.05
WB1	0.93 ± 0.34	0.68 ± 0.35	1.75	0.23
WB2	2.41 ± 1.70	1.42 ± 1.46	4.40	0.35
WB3	3.39 ± 2.54 (7.13 ± 1.88)	1.87 ± 1.49 (3.95 ± 1.39)	6.13	0.39

both cases, brittle failure involves dilatancy and shear localization. By mapping out the spatial evolution of anisotropic damage, this study provides additional insights into the interplay of stress-induced anisotropy, clustering, and localization of damage. The microstructural observations have shown that dilatancy in Darley Dale sandstone involved significant contribution from intragranular cracking (Fig. 6), that also induced ap-

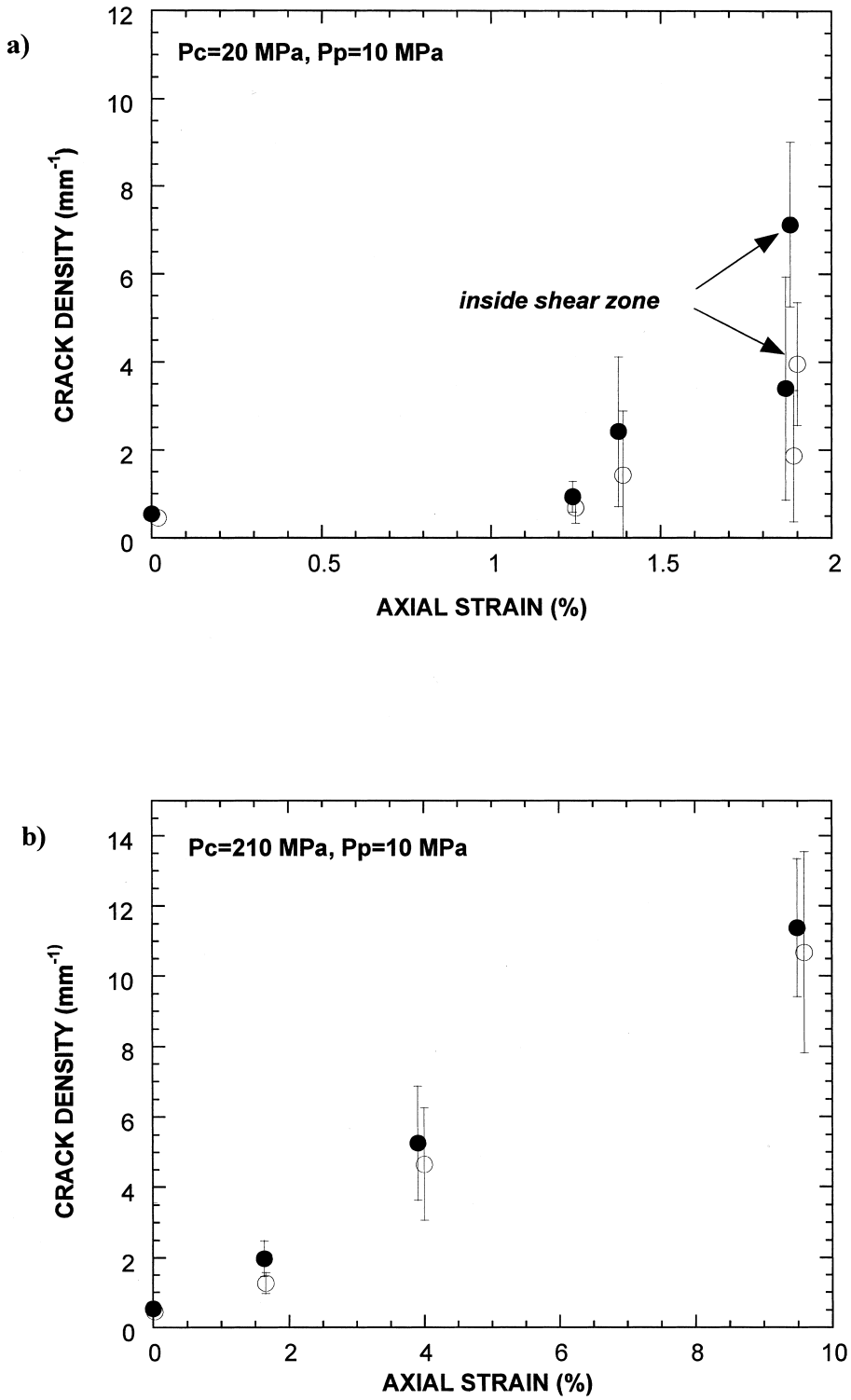

Fig. 7. Mean crack intercept densities ($P_L^{\perp}$ and $P_L^{\parallel}$) measured in directions perpendicular and parallel to the σ_1 direction. Data for the (a) WB-series and (b) WD-series are plotted as functions of the axial strain. The standard deviations are shown as error bars.

preciable stress-induced anisotropy (Fig. 7(a)). In this sense, the damage evolution is similar to that documented for very compact crystalline rocks with porosites on the order of 1%, such as the Westerly granite [4,11] and San Marcos gabbro [5]. In contrast, Menéndez et al. [15] observed that dilatancy in Berea sandstone was due to intergranular cracking and relative movement among grains, with negligible stress-induced anisotropy.

To compare the anisotropy of stress-induced cracking observed in these four rocks, we show in Fig. 12 the deformation history and microstructural data ($\Omega_{23} - \Omega_{23}^0$) of four samples that failed by brittle faulting. The stereological data for the four rocks suggest an overall trend for stress-induced anisotropy to decrease with increasing porosity. On the one hand, stress-induced anisotropy is pronounced in a compact rock, in which damage primarily arises from initiation and propagation of axial microcracks. On the other hand, stress-induced cracking is weakly anisotropic in a highly porous sandstone, in which the damage development is controlled by the contact and fracture mechanics at impinging grains. In such a cemented granular material, the direction of crack path is controlled by the remotely applied stress field as well as orientation of the grain contact normal [26].

A deeper analysis of the stereological data is not possible since the four studies were conducted with somewhat different methodologies. Although the crack sections were prepared in the same manner, the microstructural data were acquired at different magnifications (ranging from 100 to 300×). Presumably observations at higher magnifications would provide higher values for the crack densities, but since the anisotropy factor is a relative measure of crack densities, the discrepancy between studies using different magnifications may not be very significant. It should also be noted that the anisotropy factor may be sensitive to the pressure condition under which deformation occurs. The gabbro data [5] show that for samples deformed to near the peak stress, anisotropy decreases with increasing confining pressure.

4.2. Stress-induced anisotropy: theoretical prediction of the sliding wing crack model

Since dilatancy and brittle faulting in the more compact Darley Dale sandstone developed in a scenario that is akin to that in a compact crystalline rock, we compared the microstructural data on damage evolution with theoretical predictions of the sliding crack model [12–14] that has been widely used to interpret the micromechanics of brittle failure in a compact rock. In particular, we focus here on the prediction of this model on the development of stress-induced anisotropy of microcracking. A preliminary attempt to calculate the stress-induced anisotropy for the sliding wing model was made by Wong [7]. Emphasizing that

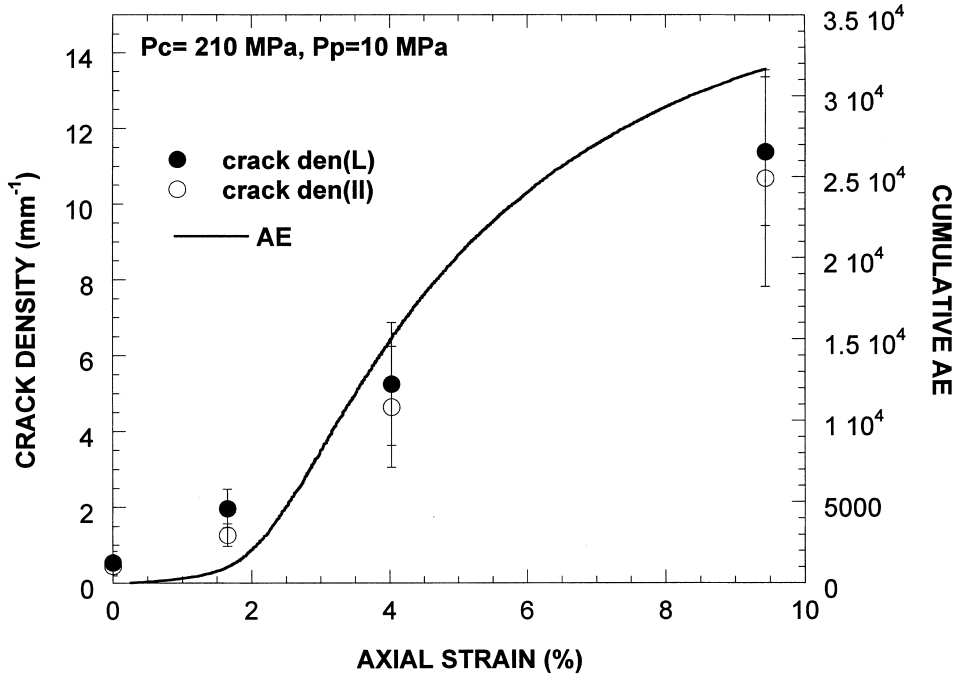

Fig. 8. Correlation between crack intercept densities and acoustic emission activity in the WD-series. The crack intercept densities ($P_L^{\perp}$ and $P_L^{\parallel}$) measured in directions perpendicular and parallel to the σ_1 direction are shown as solid and open symbols, respectively. The cumulative AE is shown as the continuous curve.

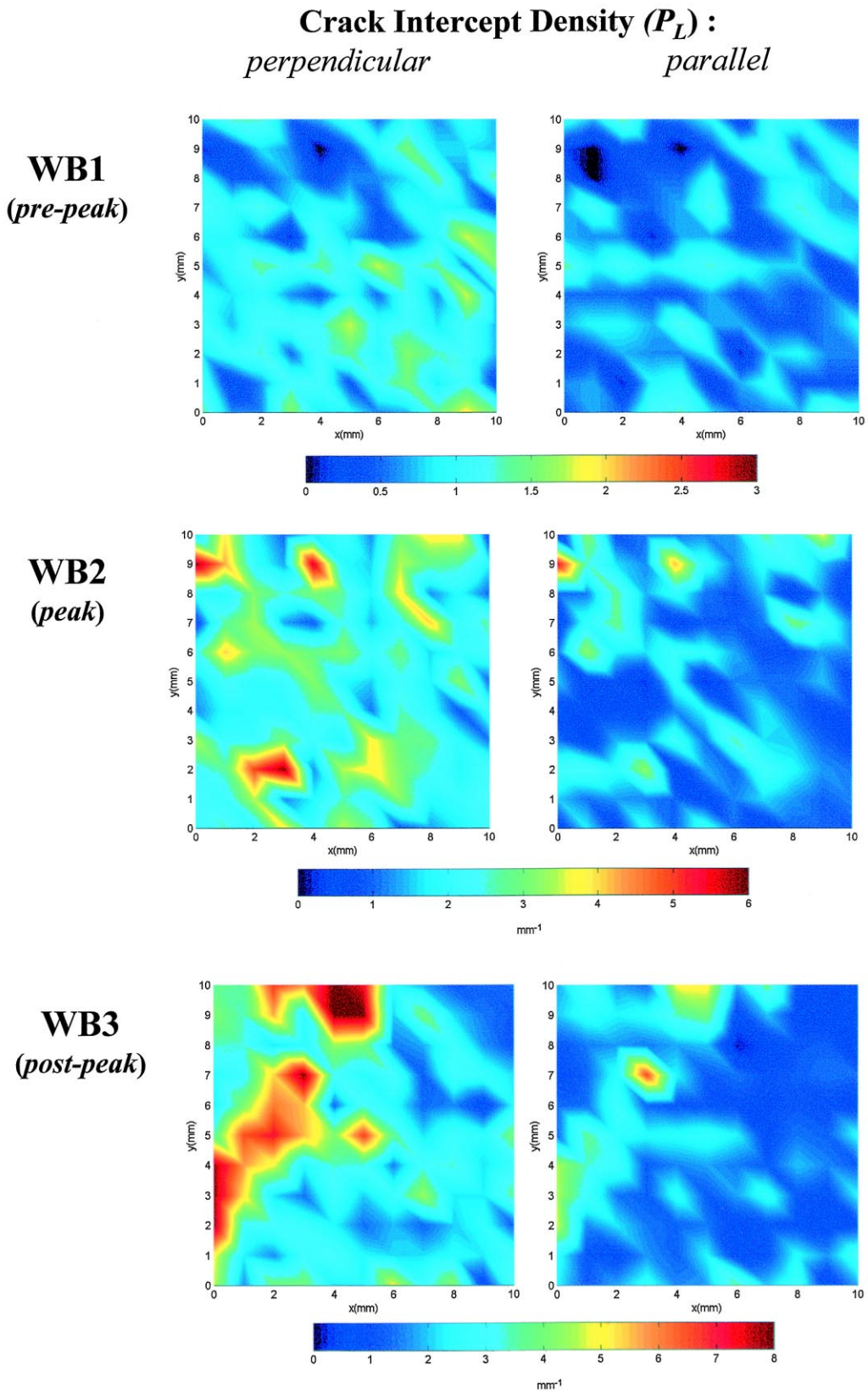

Fig. 9. Spatial distribution of crack intercept densities ($P_L^{\perp}$ and $P_L^{\parallel}$) measured in directions perpendicular and parallel to the σ_1 direction in the WB-series.

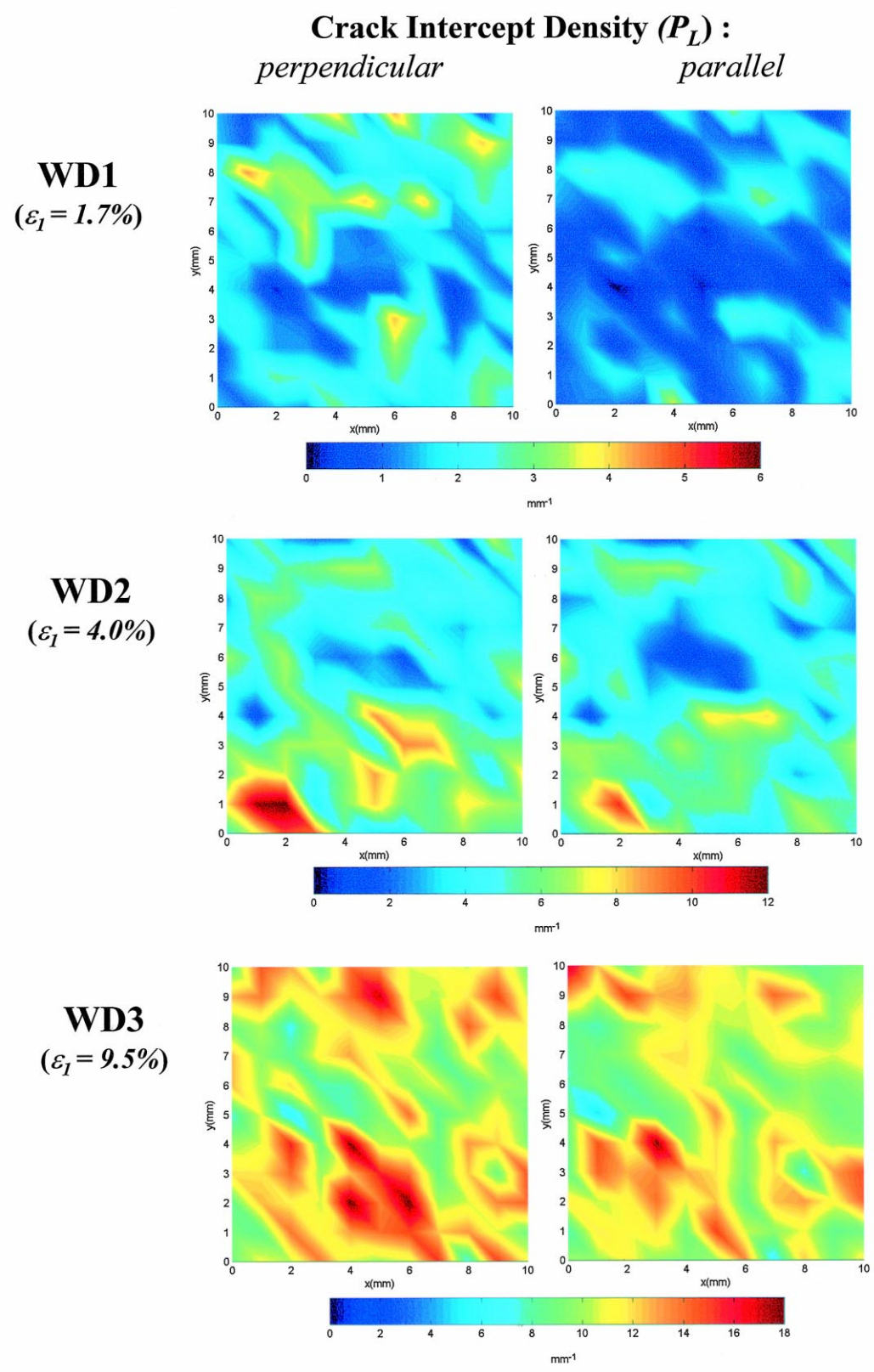

Fig. 10. Spatial distribution of crack intercept densities ($P_L^{\perp}$ and $P_L^{\parallel}$) measured in directions perpendicular and parallel to the σ_1 direction in the WD-series.

Wong's [7] approach was limited to relatively short wing cracks, Nemat-Nasser [19] suggested an improved formulation that would not be so limited. This latter formulation is used here to derive a theoretical expression for the stress-induced anisotropy.

The sliding wing crack model considers sources of tensile stress concentration that are located at the tips of pre-existing cracks (shown in Fig. 13 with length $2c$ and oriented at angle γ to σ_1). The applied stresses induce a shear traction on the crack plane and, if this resolved shear traction is sufficiently high to overcome the frictional resistance along the closed crack, frictional slip results in tensile stress concentrations at the two tips which may induce "wing cracks" to nucleate and extend out of the initial plane of the main sliding crack. The driving force is characterized by the stress

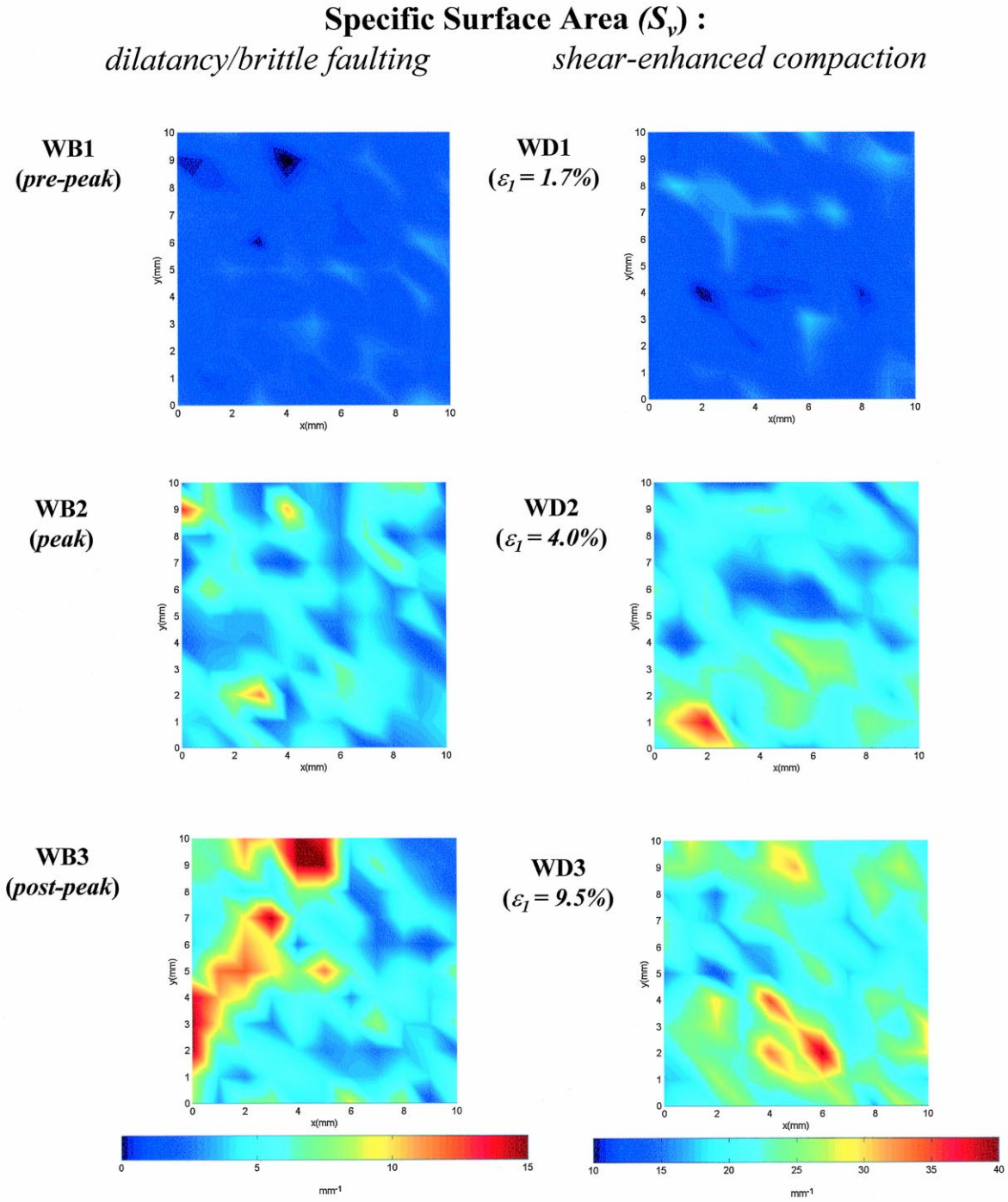

Fig. 11. Spatial distribution of specific surface area in the WB- and WD-series.

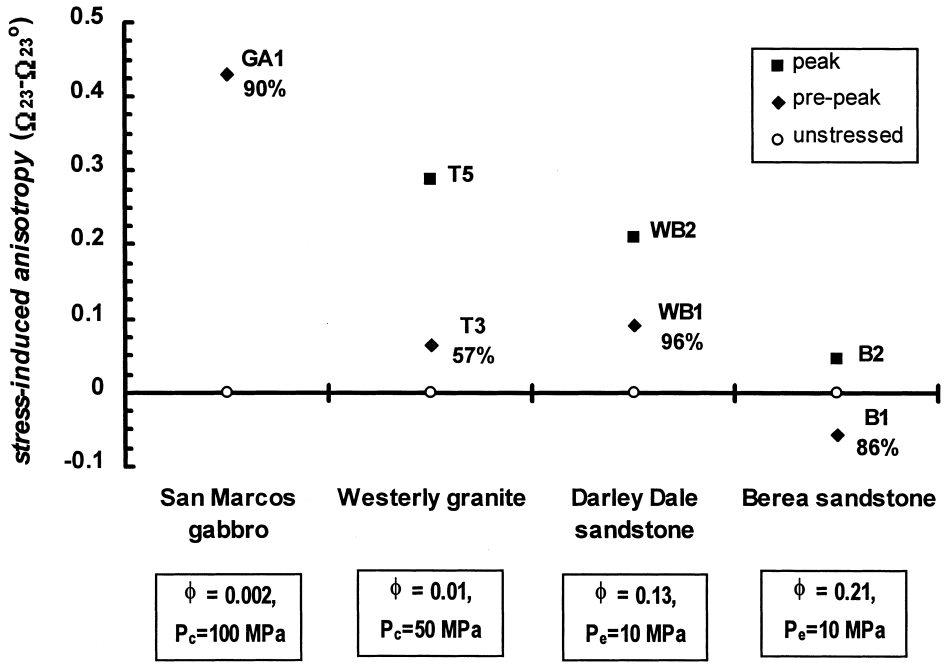

Fig. 12. Stereological data on anisotropy of stress-induced cracking in San Marcos gabbro [5], Westerly granite [2,7], Berea sandstone [15], and Darley Dale sandstone (Table 2). The samples were all deformed in the brittle faulting regime. Initial porosity and effective pressure values are shown. For each pre-peak sample, the stress level normalized to the peak stress is also indicated.

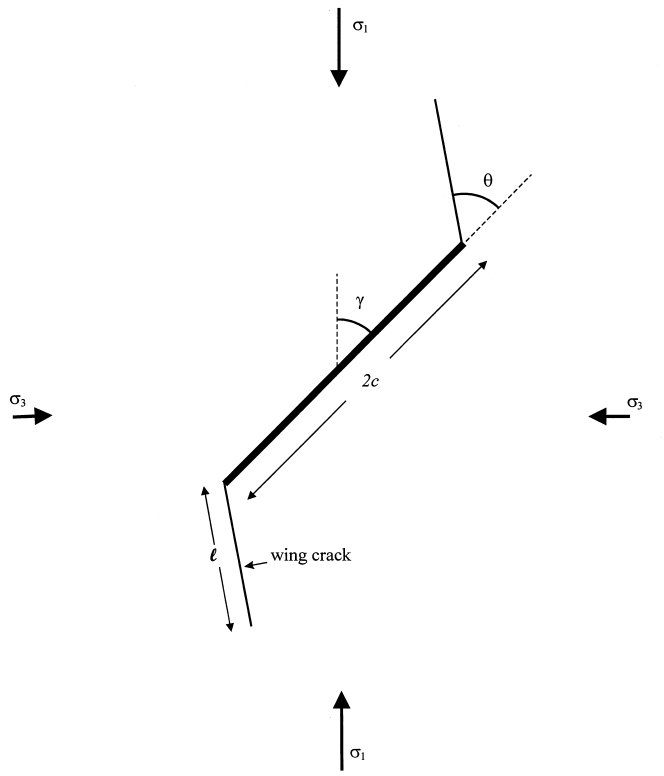

Fig. 13. Schematic diagram illustrating the geometry and loading configuration of the sliding wing crack model.

intensity factor K_I at the tip of the putative wing crack. With increased loading, it will attain the critical value K_{IC}, at which point a wing crack nucleates and propagates along a curved path to ultimately reach a stable orientation parallel to the direction of σ_1.

Wing crack initiation occurs at an angle $\theta = \cos^{-1} 1/3$ ($\approx 70.5^{\circ}$) at the stress state given by [27]:

$$\sigma_1 = \frac{\sin 2\gamma + \mu(1+\cos 2\gamma)}{\sin 2\gamma - \mu(1-\cos 2\gamma)}\sigma_3 + \frac{\sqrt{3}}{\sin 2\gamma - \mu(1-\cos 2\gamma)}\frac{K_{IC}}{\sqrt{\pi c}} \tag{3a}$$

where μ is the frictional coefficient for the main crack surface, and the angles γ and θ are defined in Fig. 13. If the onset of dilatancy C' is identified with the initiation of wing cracks and if the rock is assumed to contain randomly oriented cracks, then the wing cracks should first nucleate from those sliding cracks oriented at $\gamma = \frac{1}{2}\tan^{-1}(1/\mu)$at a stress state given by

$$\sigma_1 = \frac{\sqrt{1+\mu^2}+\mu}{\sqrt{1+\mu^2}-\mu}\sigma_3 + \frac{\sqrt{3}}{\sqrt{1+\mu^2}-\mu}\frac{K_{IC}}{\sqrt{\pi c}}. \tag{3b}$$

On the basis of extensive numerical simulations, Nemat-Nasser [12,19] derived an implicit equation to describe the evolution of a wing crack under increasing differential stress

$$\frac{(\sigma_1-\sigma_3)\sin 2\gamma-\mu[(\sigma_1+\sigma_3)-(\sigma_1-\sigma_3)\cos 2\gamma]}{\pi\sqrt{(l/c)+8/(3\pi^2)}}\sin\theta - \frac{\sqrt{(l/c)}}{2}[(\sigma_1+\sigma_3)-(\sigma_1-\sigma_3)\cos 2(\theta-\gamma)] = \frac{K_I}{\sqrt{\pi c}}. \quad (4)$$

The wing crack orientation is given by the value of θ (Fig. 13) that maximizes the above expression for the stress intensity factor K_I, and the crack length l is then calculated by setting $K_I = K_{IC}$. The calculation requires appropriate values of the parameters μ and $K_{IC}/\sqrt{\pi c}$ for the rock of interest. In previous studies, these parameters were adjusted to fit mechanical data. Here we use linear regression on the stress data at the onset of dilatancy to obtain parameter values that are

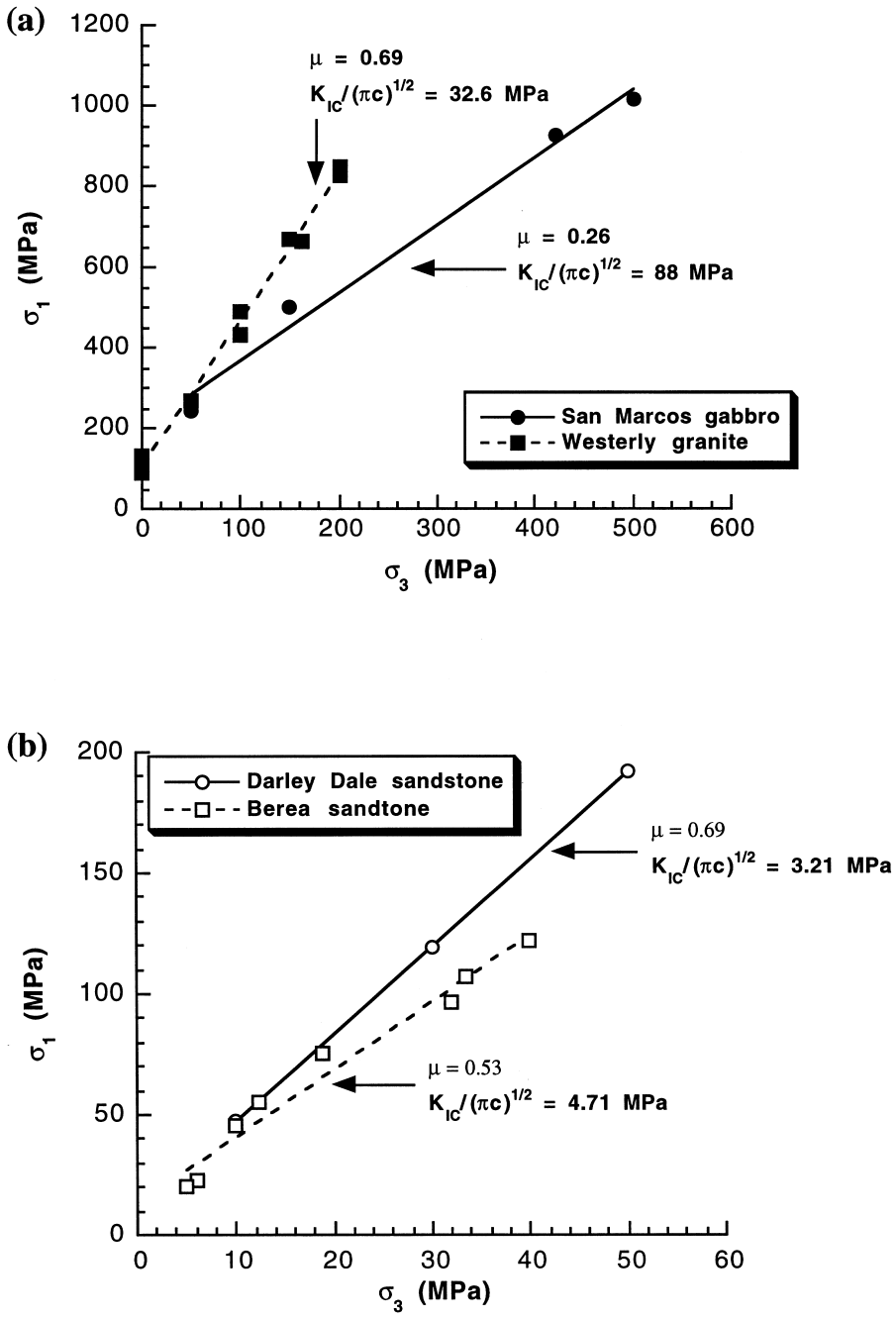

Fig. 14. Triaxial compression data for the principal stresses at the onset of dilatancy of (a) San Marcos gabbro [29], Westerly granite [28], (b) Berea sandstone and Darley Dale sandstone [17]. The mechanical data were fitted to Eq. (3b), and the linear regression results are also shown.

consistent with Eq. (3b). The parameter values can then be substituted into Eq. (4) to calculate the ratio l/c as a function of the angle γ for a given set of principal stresses σ_1 and σ_3.

Further assumptions are necessary before the theoretical model can be related to the stereological measurements. If the pore space is assumed to be made up of an ensemble of sliding wing cracks, then it can be shown that the stress-induced anisotropy factor is related to the mean crack lengths [7]

$$\Omega_{23} - \Omega_{23}^0 = \frac{\langle l \rangle}{\langle l + c \rangle} \approx \frac{\langle l/c \rangle}{1 + \langle l/c \rangle} \tag{5}$$

where Ω_{23} and Ω_{23}^0 are the anisotropy factors for the deformed and unstressed samples, respectively and the assumption is made that the crack half-length c spans a relatively narrow range.

4.3. Development of stress-induced anisotropy in compact and porous rocks

Mechanical data of Westerly granite [28], San Marcos gabbro [29], Berea sandstone and Darley Dale sandstone (Fig. 14(a) and (b)) for the onset of dilatancy follow approximately linear trends in the principal stress space. Fitting the data to Eq. (3b), the parameters μ and $K_{IC}/\sqrt{\pi c}$ were estimated by linear regression (Table 3). The inferred values for friction coefficient fall in typical ranges for quartz and feldspar [30], except for San Marcos gabbro that has the lowest value of $\mu = 0.26$, possibly because its modal composition includes a relatively high percentage of biotite that has anomalously low friction coefficient among silicate minerals.

The inferred values of the ratio $K_{IC}/\sqrt{\pi c}$ for the two compact rocks are considered to be reasonable. Since significant proportion of stress-induced cracks were observed to be intragranular in the granite and gabbro, a plausible value for fracture toughness at the onset of dilatancy would be that for a cleavage plane of feldspar, with $K_{IC} \sim 0.4$ MPa $m^{1/2}$ [31]. To be consistent with the linear regression results in Fig. 14(a), this fracture toughness value requires that the pre-existing crack lengths $2c$ should be ~90 μm for Westerly granite, that is comparable to that of the longest cracks (100–500 μm) for an unstressed sample reported by Hadley [32]. The corresponding value is $2c \sim 10$ μm for San Marcos gabbro, that is significantly shorter than the average grain size (~2 mm). However, since most of the grain boundaries in this gabbro were observed to be sealed [5] this relative low value of $2c$ is not unreasonable.

In comparison, values of the ratio $K_{IC}/\sqrt{\pi c}$ for the two porous sandstones are significantly lower. Even if we assume upper-bound values of $2c$ comparable to the grain sizes of Berea sandstone (0.17 mm) and Darley Dale sandstone (0.22 mm), the linear regression results of Fig. 14(b) imply that $K_{IC} \leq 0.1$ MPa $m^{1/2}$, which is significantly lower than values for common minerals [31]. Such low values are plausible only for weakly cohesive grain boundaries.

Substituting these parameter values of μ and $K_{IC}/\sqrt{\pi c}$ into Eqs. (4) and (5), the stress-induced anisotropy was calculated as a function of the crack angle γ for a sample of each rock at the peak stress (Fig. 15). For comparison the maximum values predicted by the sliding wing crack model (from Fig. 15) and stereological data (Fig. 12) are compiled in Table 3. Theoretical estimates of the stress-induced anisotropy are significantly lower than the microstructural measurements for the compact rocks and higher for the porous sandstones, respectively.

For the highly porous Berea sandstone, the discrepancy with microstructural observation is not surprising since the microstructural observations indicate that it is unlikely the wing crack model is applicable even as a qualitative analogue for brittle failure in this cemented granular material. However, the significant discrepancies in the other three rocks are somewhat unexpected, since the wing crack model seems to capture the micromechanics of brittle faulting in these cases and the theoretical expressions adopted here are considered to be more accurate [12,19]. We have conducted additional parametric studies which show that the wing crack model predictions agree with the microstructural data of Westerly granite only if a friction coefficient of ~0.1 is assumed. Such a value is considered to be anomalously low for common minerals and significantly smaller than that inferred from mechanical data on the onset of dilatancy (Table 3). In a related application of the wing crack model, Nemat-Nasser and Obata [33] have also concluded that par-

Table 3
Comparison of parameters inferred from wing crack model and microstructural measurements

Rock type	μ	$K_{IC}\sqrt{\pi a}$ (MPa)	P_e (MPa)	$\Omega_{23} - \Omega_{23}^0$ (measured)	$\Omega_{23} - \Omega_{23}^0$ (calculated)
San Marcos gabbro	0.26	88.0	100	> 0.49	0.139
Westerly granite	0.69	33.0	50	0.28	0.132
Darley Dale sandstone	0.69	3.21	10	0.24	0.330
Berea sandstone	0.53	4.71	10	0.05	0.327

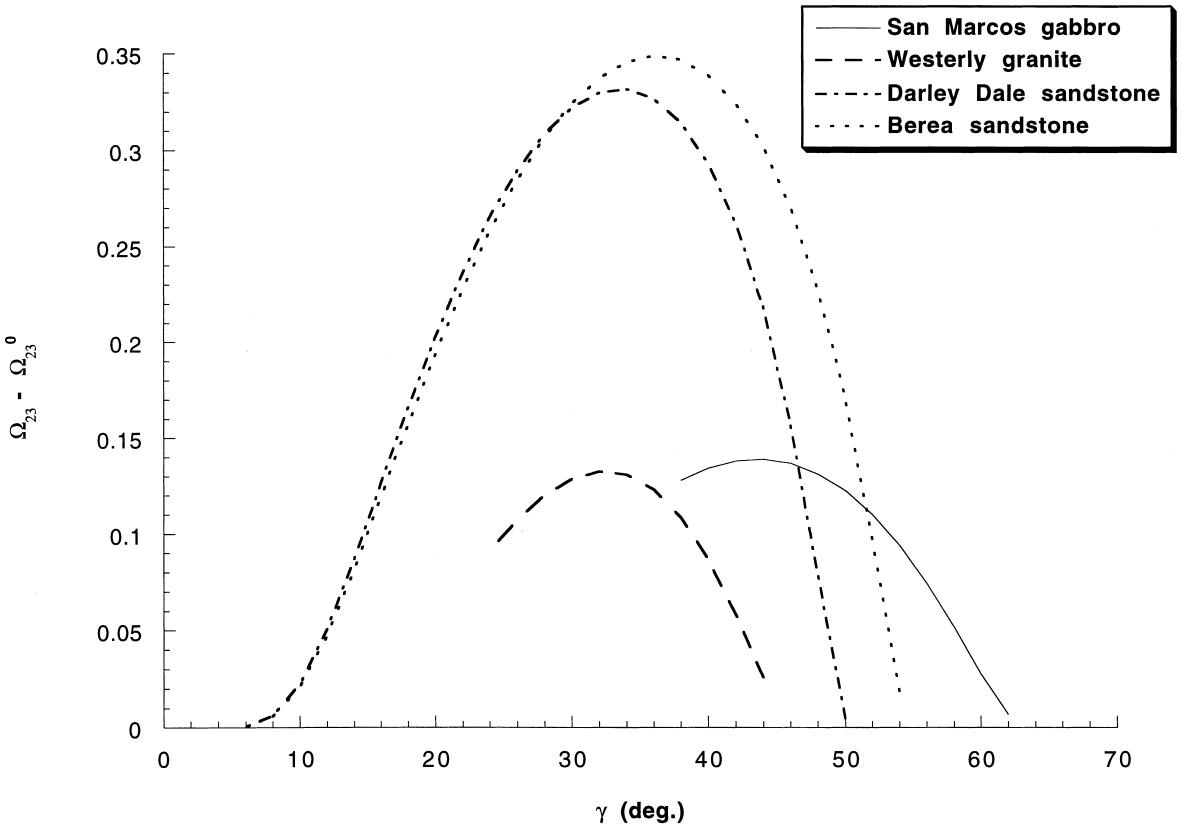

Fig. 15. Theoretical predictions of the stress-induced anisotropy at the peak stress levels for San Marcos gabbro, Westerly granite, Darley Dale sandstone, and Berea sandstone. Eqs. (4) and (5) were used, assuming values of μ and $K_{IC}/\sqrt{\pi c}$ in Fig. 13. Theoretical values are available only for sliding cracks with angles γ optimally oriented for wing crack initiation.

ameter values of $\mu = 0.1$ (and $K_{IC}/\sqrt{\pi c} = 25$ MPa) were required to fit volumetric strain data during the development of dilatancy in Westerly granite.

Kemeny and Cook [14] as well as Nemat-Nasser [19] have emphasized that since the growth behavior of a wing crack is qualitatively similar to that induced by stress concentrations arising from other mechanisms (such as elastic mismatch or equidimensional voids), it provides a useful mathematical analogue for analyzing the micromechanics of brittle failure in a compact rock. Nevertheless, it should be kept in mind that the sliding crack represents a semi-quantitative analogue of a variety of mechanisms operative during the development of dilatancy. In the wing crack model the parameter μ is used as an "effective" parameter to characterize the overall stress concentration due to these various mechanisms, and consequently μ may not exactly correspond to actual values of friction coefficient on sliding crack surfaces in the rock.

It should also be noted that we have not considered how stress-induced anisotropy depends on crack interaction effect [12–14,34–36], which may be relevant in the vicinity of the peak stress and is definitely crucial in the strain softening stage. Furthermore a two-dimensional geometry is assumed for wing crack growth. Recent three-dimensional results of Germanovich et al. [37] have underscored a number of differences that arise from geometric complexity, which should be considered in future theoretical analysis of anisotropic damage development.

Acknowledgements

We are grateful to Richard Yund for the use of the ion-milling facilities at Brown University. We also thank Joanne Fredrich, Leonid Germanovich, Philip Meredith, and Veronika Vajdova for helpful discussions and thoughtful reviews. This research was partially supported by the Office of Basic Energy Sciences, Department of Energy, under grant DEF-G0294ER14455. This paper is dedicated to Neville G. W. Cook, whose fundamental research over several decades has contributed significantly to many of the rock mechanics areas discussed.

References

[1] Hallbauer DK, Wagner H, Cook NGW. Some observations concerning the microscopic and mechanical behavior of quartzite specimens in stiff, triaxial compression tests. Int J Rock Mech Min Sci & Geomech Abstr 1973;10:713–26.

[2] Tapponier P, Brace WF. Development of stress-induced microcracks in Westerly granite. Int J Rock Mech Min Sci & Geomech Abstr 1976;13:103–12.

[3] Kranz RL. Crack growth and development during creep in Westerly granite. Int J Rock Mech Min Sci & Geomech Abstr 1979;16:23–36.

[4] Wong T-f. Micromechanics of faulting in Westerly granite. Int J Rock Mech Min Sci & Geomech Abstr 1982;19:49–64.

[5] Wong T-f, Biegel R. Effects of pressure on the micromechanics of faulting in San Marcos gabbro. J Struct Geol 1985;7:737–49.

[6] Kranz RL. Microcracks in rocks, a review. Tectonophysics 1983;100:449–80.

[7] Wong T-f. Geometic probability approach to the characterization and analysis of microcracking in rocks. Mech Mat, 1985;4:261–76.

[8] Soga N, Mizutani H, Spetzler H, Martin RJ. The effect of dilatancy on velocity anisotropy in Westerly granite. J Geophys Res 1978;83:4451–8.

[9] Trimmer D, Bonner B, Heard HC, Duba A. Effect of pressure and stress in water transport in intact and fractured gabbro and granite. J Geophys Res 1980;85:7059–71.

[10] Lockner DA, Byerlee JD, Kuksenko V, Ponomarev A, Sidorin A. Observations of quasistatic fault growth from acoustic emissions. In: Evans B, Wong T-f, editors. Fault mechanics and transport properties of rocks. San Diego, CA: Academic, 1992. p. 3–32.

[11] Moore DE, Lockner DA. The role of microcracking in shear-fracture propagation in granite. J Struct Geol 1995;17:95–114.

[12] Horii H, Nemat-Nasser S. Brittle failure in compression: splitting, faulting and brittle-ductile transition. Phil Trans Royal Soc London 1986;319:337–74.

[13] Ashby MF, Sammis CG. The damage mechanics of brittle solids in compression. PAGEOPH 1990;133:489–521.

[14] Kemeny JM, Cook NGW. Micromechanics of deformation in rocks. In: Shah SP, editor. Toughening mechanisms in quasi-brittle materials. Klewer Academic, 1991. p. 155–88.

[15] Menéndez B, Zhu W, Wong T-f. Micromechanics of brittle faulting and cataclastic flow in Berea sandstone. J Struct Geol 1996;18:1–16.

[16] Read MD, Ayling MR, Meredith PG, Murrell SAF. Microcracking during triaxial deformation of porous rocks monitored by changes in rock physical properties. II. Pore volumometry and acoustic emission measurements on water-saturated rocks. Tectonophysics 1995;245:223–36.

[17] Wong T-f, David C, Zhu W. The transition from brittle faulting to cataclastic flow in porous sandstones: mechanical deformation. J Geophys Res 1997;102:3009–25.

[18] Zhu W, Wong T-f. The transition from brittle faulting to cataclastic flow: permeability evolution. J Geophys Res 1997;102:3027–41.

[19] Nemat-Nasser S. Discussion of geometric probability approach to the characterization and analysis of microcracking in rocks. Mech Mater 1985;4:277–81.

[20] Curran JH, Carroll MM. Shear stress enhancement of void compaction. J Geophys Res 1979;84:1105–12.

[21] Richter D, Simmons G. Microcracks in crustal igneous rocks: microscopy. In: Heacock JG, editor. The earth's crust: its nature and physical properties. Washington, DC: AGU, 1977. p. 149–80.

[22] Brace WF, Silver E, Hadley K, Goetze C. Cracks and pores — a close look. Science 1972;178:163–5.

[23] Underwood EE. In: Quantitative stereology. Reading: Addison Wesley, 1970. p. 274.

[24] Russ JC. In: Practical stereology. NY: Plenum, 1986. p. 185.

[25] Zhang J, Wong T-f, Davis DM. Micromechanics of pressure-induced grain crushing in porous rocks. J Geophys Res 1990;95:341–52.

[26] Shah KR, Wong T-f. Fracturing at contact surfaces subjected to normal and tangential loads. Int J Rock Mech Min Sci & Geomech Abstr 1997;34:722–39.

[27] Cotterell B, Rice JR. Slightly curved or kinked cracks. Int J Fracture 1980;16:155–69.

[28] Brace WF, Paulding B, Scholz CH. Dilatancy in the fracture of crystalline rocks. J Geophys Res 1966;71:3939–54.

[29] Hadley K. The effect of cyclic stress on ditatancy: another look. J Geophys Res 1976;81:2471–4.

[30] Horn HM, Deere DU. Frictional characteristics of minerals. Geotechnique 1962;12:319–35.

[31] Atkinson BK, Meredith PG. Experimental fracture mechanics data for rocks and minerals. In: Atkinson BK, editor. Fracture mechanics of rock. London: Academic Press, 1987. p. 477–525.

[32] Hadley K. Comparison of calculated and observed crack densities and seismic velocities in Westerly granite. J Geophys Res 1976;81:3484–94.

[33] Nemat-Nasser S, Obata M. A microcrack model of dilatancy in brittle materials. J App Mech 1988;55:24–35.

[34] Baud P, Reuschle T. A theoretical approach to the propagation of interacting cracks. Geophys J Int 1997;130:460–8.

[35] Lee X, Ju JW. Micromechanical damage models for brittle solids. II: compressive loadings. J Eng Mech 1991;117:1515–36.

[36] Okui Y, Horii H. Stress and time-dependent failure of brittle rocks under compression: a theoretical prediction. J Geophys Res 1997;102:14,869–81.

[37] Germanovich LN, Salganik RL, Dyskin AV, Lee KK. Mechanisms of brittle fracture of rock with pre-existing cracks in compression. Pure Appl Geophys 1994;143:117–49.